ChemSusChem

Research Article
doi.org/10.1002/cssc.202300934

Chemistry Europe
European Chemical Societies Publishing

www.chemsuschem.org

Tailoring Cu Electrodes for Enhanced CO_2 Electroreduction through Plasma Electrolysis in Non-Conventional Phosphorus-Oxoanion-Based Electrolytes

Mohamed M. Elnagar[+],[a] Pramod V. Menezes[+],[a] Walter A. Parada[+],[b] Yannick Mattausch,[a] Ludwig A. Kibler,[a] Karl J. J. Mayrhofer,[b] and Timo Jacob*[a, c, d]

This study presents a green, ultra-fast, and facile technique for the fabrication of micro/nano-structured and porous Cu electrodes through in-liquid plasma electrolysis using phosphorous-oxoanion-based electrolytes. Besides the preferential surface faceting, the Cu electrodes exhibit unique surface structures, including octahedral nanocrystals besides nanoporous and microporous structures, depending on the employed electrolyte. The incorporation of P-atoms into the Cu surfaces is observed. The modified Cu electrodes display increased roughness, leading to higher current densities for CO_2 electroreduction reaction. The selectivity of the modified Cu electrodes towards C_2 products is highest for the Cu electrodes treated in Na_2HPO_3 and Na_3PO_4 electrolytes, whereas those treated in $Na_2H_2PO_2$ produce the most H_2. The Cu electrode treated in Na_3PO_4 produces ethylene (23%) at −1.1 V vs. RHE, and a comparable amount of acetaldehyde (15%) that is typically observed for Cu(110) single crystals. The enhanced selectivity is attributed to several factors, including the surface morphology, the incorporation of phosphorus into the Cu structure, and the formation of Cu(110) facets. Our results not only advance our understanding of the influence of the electrolyte's nature on the plasma electrolysis of Cu electrodes, but also underscores the potential of in-liquid plasma treatment for developing efficient Cu electrocatalysts for sustainable CO_2 conversion.

Introduction

The electrochemical reduction of CO_2 (CO_2RR) offers an attractive route to sustainably upgrade captured CO_2 into value-added multicarbon (C_{2+}) products.[1–4] The actual reaction pathway in CO_2RR strongly depends on the chemical nature and surface structure of the working electrode. In this respect, Cu-based electrocatalysts demonstrate outstanding electrocatalytic performance for the conversion of CO_2 into C_{2+} products, as they feature an adjustable coordination environment and moderate binding affinity with intermediates such as adsorbed carbon monoxide, CO_{ad}.[5,6] Commercial Cu foils and wires are the most widely used as affordable Cu-based catalysts for CO_2 electroreduction. However, they suffer from very low C_{2+} selectivity due to the difficulty of C–C coupling and the concurrent hydrogen evolution reaction (HER), limiting their further use.[1,7,8]

The electrocatalytic activity and selectivity of Cu electrodes are strongly correlated with their surface structure (*i.e.*, surface morphology, roughness, grain boundaries, crystal facets, defects, and heteroatom doping), and chemical state (*e.g.*, subsurface oxygen and Cu(I) species).[8–12] Thus, to improve the selectivity for C_{2+} products and suppress competitive HER, various nanostructured Cu catalysts have been developed by engineering low-coordinated sites and increasing surface roughness.[1,9,13–16]

Controlling the formation of surface oxide species and the adsorption of intermediates in CO_2 electroreduction is also proven to be an effective strategy to enhance the selectivity of Cu electrodes for desired products. In this context, oxide-derived Cu has shown an increased selectivity for the electrocatalytic reduction of CO_2 to multi-carbon products rather than methane.[17–20] A fundamental understanding of the remarkable catalytic activity of oxide-derived Cu catalysts is still lacking and the main reasons are under intense debate. Most likely, the extraordinarily high electrocatalytic activity is possibly related to the nanostructured surface of the catalyst formed by the reduction of the surface oxide, which provides low-coordinated atoms as active sites, subsurface oxygen, grain boundaries, exposed facets, and local pH variations.[19,21–25]

Based on the aforementioned aspects, surface engineering of Cu electrodes through the combination of controlled surface

[a] *M. M. Elnagar,[+] Dr. P. V. Menezes,[+] Y. Mattausch, Dr. L. A. Kibler, Prof. Dr. T. Jacob*
Institute of Electrochemistry, Ulm University, 89069 Ulm (Germany)

[b] *W. A. Parada,[+] Prof. Dr. K. J. J. Mayrhofer*
Helmholtz Institute Erlangen-Nürnberg for Renewable Energy (HI ERN), Egerlandstr. 3, 91058 Erlangen (Germany)

[c] *Prof. Dr. T. Jacob*
Helmholtz-Institute-Ulm (HIU) Electrochemical Energy Storage, 89081 Ulm, Germany

[d] *Prof. Dr. T. Jacob*
Karlsruhe Institute of Technology (KIT), P.O. Box 3640, 76021 Karlsruhe (Germany)
E-mail: timo.jacob@uni-ulm.de

[+] *These authors contributed equally to this work.*

Supporting information for this article is available on the WWW under https://doi.org/10.1002/cssc.202300934

morphology and formation of oxides (*i.e.*, Cu_xO or CuO) or oriented facets, *e.g.*, (111) or (100) is highly desired in order to tailor the catalytic activity and to enhance the surface area, thus increasing the CO_2 electroreduction performance for C_{2+} products. Diverse catalyst engineering approaches have been advanced to improve the electrocatalytic performance of Cu for CO_2 electroreduction through the fabrication of nanostructured and oxide-derived Cu catalysts.[1,2,12,15,26] Alternatively, in-liquid (gas-liquid dual phase) plasma electrolysis, in which the metallic electrodes are immersed into a definite electrolyte and processed by continuous sparking under a relatively high applied voltage, holds promise as a powerful, affordable, green, and ultra-fast technique for tailoring the surface structure of metal electrodes.[27–33]

Fascinatingly, in-liquid plasma enables the formation of metal surfaces with a high degree of porosity and tunable morphology and chemical state, as well as a controllable oxide film, depending on the experimental conditions such as the electrolyte composition, electrode material, and applied voltage.[27–30] During plasma electrolytic oxidation, the electrolyte supplies high electrical conductivity and induces a particular surface anodization reaction, leading to the growth of its oxide or hydroxide films with specific morphology and chemical state.[30,34,35]

The addition of nanoparticles such as SiO_2, Si_3N_4, TiO_2, ZrO_2, Ag, and CeO_2 to the alkaline electrolyte during plasma-anodization of the metal electrodes can significantly affect the resulting anodized films' structural and chemical properties as well as the plasma operating parameters.[30,36,37] For example, recently, we have shown that the active incorporation of SiO_2 nanoparticles (11 nm) during plasma electrolysis results in the growth of 3D coral-like microstructures on Cu electrodes accompanied by a remarkable increase in the electrochemically active surface area (EASA).[30] On the other hand, the influence of the electrolyte anions on the plasma operating parameters and the final surface structure of plasma-treated metal electrodes has not yet been explored. Additionally, while gas-phase plasma has been employed for the activation of Cu catalysts for CO_2 electroreduction,[12,20,38] the in-liquid plasma approach has not yet been employed for this purpose. Providing further insights into these aspects can enhance our understanding of the plasma-anodization process and its potential applications.

In this contribution, we present a facile, green, and ultra-fast one-step approach to fabricate novel micro/nanostructured and porous Cu electrodes through plasma electrolysis utilizing non-conventional P-based electrolytes, including sodium hypophosphite (NaH_2PO_2), sodium hydrogen phosphite (Na_2HPO_3), and sodium phosphate (Na_3PO_4). Notably, the plasma operating parameters and the final surface structure of Cu electrodes are strongly influenced by the nature of the electrolyte anions. Changes in the surface morphology, chemical composition, electrochemically active surface area (EASA), and electrochemical behavior of the Cu electrodes as a function of electrolyte nature at various applied voltages are systematically investigated. Scanning electron microscopy (SEM) micrographs reveal that plasma treatment of the Cu surfaces generates octahedral nanocrystals using NaH_2PO_2, a nano-porous structure using Na_2HPO_3, and a micro-porous structure using Na_3PO_4, all exhibiting characteristic Cu facets. Moreover, plasma electrolysis not only results in the formation of an oxide layer but also induces the incorporation of P-atoms into the Cu surface. The important role of the electrolyte anions in the nanostructuring of the Cu surfaces is considered and demonstrated. To shed light on the relative effect of the above-mentioned parameters, we investigate the electrocatalytic activity of the modified Cu electrodes towards CO_2 electroreduction and observe enhanced selectivity for carbon-to-carbon coupling products such as ethylene, acetaldehyde, and 1-propanol. By utilizing the fundamental insights gained from the present study, it becomes possible to explore new avenues and strategies for the design and engineering of Cu surfaces. These insights can be leveraged to enhance the performance of Cu electrodes in various electrocatalytic reactions, with a specific focus on improving their efficiency and selectivity in CO_2 electroreduction.

Results and discussion

I–U characteristics

Investigating the influence of the electrolyte composition on the plasma electrolysis with Cu wire anodes provides valuable insights on how to engineer their surface structure for tuning the electrocatalytic performance. In this study, plasma electrolysis was performed using a simple asymmetric two-electrode system with Cu anodes, as schematically illustrated in Figure 1a. The stationary current-voltage (*I–U*) behavior of the Cu wire electrodes recorded for 15 s electrolysis in 0.01 M NaH_2PO_2 (pH = 7.3), 0.01 M Na_2HPO_3 (pH = 8.6), and 0.01 M Na_3PO_4 (pH = 11.7) is shown in Figure 1b. The average current values over different voltages (50–600 V) were measured using freshly polished Cu electrodes and electrolytes for each voltage. For all studies, the initial temperature of the electrolyte was maintained at 30 °C.

The *I–U* characteristics can be systematically divided into four stages,[30,39,40] however, the voltage regime for the same stage is different in response to the nature of the electrolyte anions. In the normal electrolysis region (up to about 250 V, 300 V, and 550 V for Na_3PO_4, Na_2HPO_3, and NaH_2PO_2, respectively), the current increases linearly as a function of the applied voltage according to Ohm's law in relation to the conductivity of the electrolyte.[41] During this stage, a gaseous sheath develops around the electrode/electrolyte interface, in which bubble formation increases significantly with increasing voltage. At the peak of the *I–U* curve (250 V, 300 V, and 550 V for Na_3PO_4, Na_2HPO_3, and NaH_2PO_2, respectively), known as the breakdown voltage, the continuous gaseous sheath covers the entire electrode surface, hindering Faraday reactions at the interface. Further increase in the applied voltages leads to a gradual decrease in the current (the third stage) due to the high electrical resistance of the gaseous envelopes and the decrease in effective interfacial area. Notably, a uniform plasma discharge with intense light emission is observed in the O_2 gas bubble region of the anode (the fourth stage), as schematically

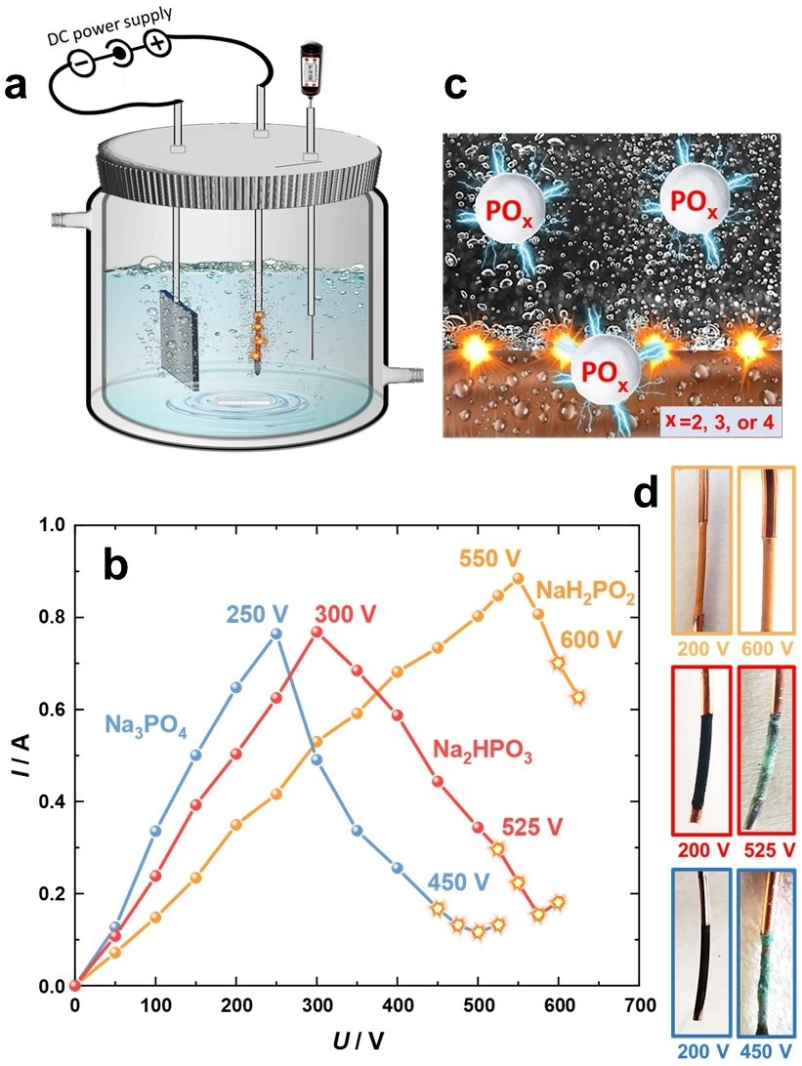

Figure 1. Plasma electrolysis process. a) Schematic illustration of a two-electrode plasma electrolysis system. b) Current-voltage curves for the electrolysis of 0.01 M NaH_2PO_2 (orange), Na_2HPO_3 (red), or Na_3PO_4 (blue) electrolyte with Cu wire electrodes. c) Schematic illustration of the Cu surfaces during plasma electrolysis. d) Optical graphs of the corresponding Cu wires after electrolysis for 15 s in two regimes (200 V and plasma regime).

demonstrated in Figure 1c, at $U \geq 450$ V, 525 V, and 600 V during electrolysis in Na_3PO_4, Na_2HPO_3, and NaH_2PO_2, respectively. The plasma regime is highlighted by open star symbols (Figure 1b). Going beyond 525 V in the case of Na_3PO_4, and 600 V in the case of both Na_2HPO_3 and NaH_2PO_2 results in the melting of the wire due to the extreme heat generated by the continuous plasma glow discharge. The electric conductivities of 0.01 mol·L^{-1} NaH_2PO_2, Na_2HPO_3, and Na_3PO_4 at 30 °C are 899 μS·cm^{-1}, 1830 μS·cm^{-1}, and 3320 μS·cm^{-1}, respectively. Thus, shifts in the *I–U* characteristics of the Cu anodes during electrolysis as a function of the electrolyte identity, in which each stage emerges at distinctly different voltage regimes, are due to their different electrolyte properties including electric conductivity, heat capacity, viscosity, etc.

Figure 1d shows optical images of the Cu wires after normal electrolysis and plasma electrolysis in the three employed electrolytes. Visibly, a remarkable decrease in the diameter of the Cu wires is noticed after electrolysis in NaH_2PO_2 revealing a significant dissolution of Cu, which is more pronounced for normal electrolysis compared to plasma electrolysis. The severe dissolution of Cu electrodes is possibly caused by the chemical reduction of CuO (formed during electrolysis) by $H_2PO_2^-$ ions.[42] One possibility, among others, is illustrated according to the following reaction [Eq. (1)], while the actual reaction mechanism is certainly more complex under the conditions of electrolysis.

$$2\ CuO + H_2PO_2^- \rightarrow 2\ Cu + H_2PO_4^- \quad (1)$$

The Cu wires turn black after normal electrolysis and light bluish-green after plasma electrolysis of both Na_2HPO_3 and Na_3PO_4. Phosphate anions strongly interact with Cu(II) forming salts and complexes in an aqueous solution. Various thermodynamically stable complexes can form, such as $Cu(HPO_4)$, $[Cu(H_2PO_4)]^+$, sparingly soluble precipitates of Cu(II) phosphate $Cu_3(PO_4)_2$, and several hydrolyzed forms such as libethenite $Cu_2(PO_4)(OH)$, cornetite $Cu_3(PO_4)(OH)_3$, reichenbachite

$Cu_5(PO_4)_2(OH)_4$, and pseudomalachite $Cu_5(PO_4)_2(OH)_4.H_2O$.[43–47] The light bluish-green color of the Cu wires after plasma electrolysis indicates the formation of $Cu_3(PO_4)_2$, which is insoluble in water and thus is deposited at the electrode surface. Based on these observations, it seems that Na_2HPO_3 is oxidized to Na_3PO_4 at the electrolyte/electrode interface during plasma electrolysis, leading to the formation of $Cu_3(PO_4)_2$. On the other hand, the reduction of Cu^{2+} upon electrolysis of NaH_2PO_2 might be the reason for the disappearance of Cu(II) phosphate.

The employed P-based electrolytes have different pH values. Therefore, we increased the pH of NaH_2PO_2 from 7.3 to 11.7 using NaOH to have the same pH of Na_3PO_4 and to understand the influence of the pH on the electrolysis of Cu electrodes. While the *I–U* behavior is distinguishable from both NaH_2PO_2 and Na_3PO_4 (Figure S1a), similar dissolution behavior of Cu wires is observed independent of pH (Figure S1b). Accordingly, these results indicate that the nature of the electrolyte and its conductivity are the dominant parameters controlling electrolysis with Cu wire anodes.

Surface characterization

We have systematically monitored the evolution of the surface morphology and composition of the Cu electrodes after anodic polarization in 0.01 M NaH_2PO_2, Na_2HPO_3, and Na_3PO_4 at various voltages for 15 s. Figures 2a–l compare the surface morphology of the electrodes polarized in the normal electrolysis regime (100 V) and the plasma electrolysis regime. Additional SEM images illustrating systematically the effect of the applied voltages on the surface morphology are shown in Figures S2–S5.

As shown in Figures S2a–c, Cu dissolution is detected after anodic polarization but to a different extent depending on the nature of the electrolyte and the applied voltage. To illustrate

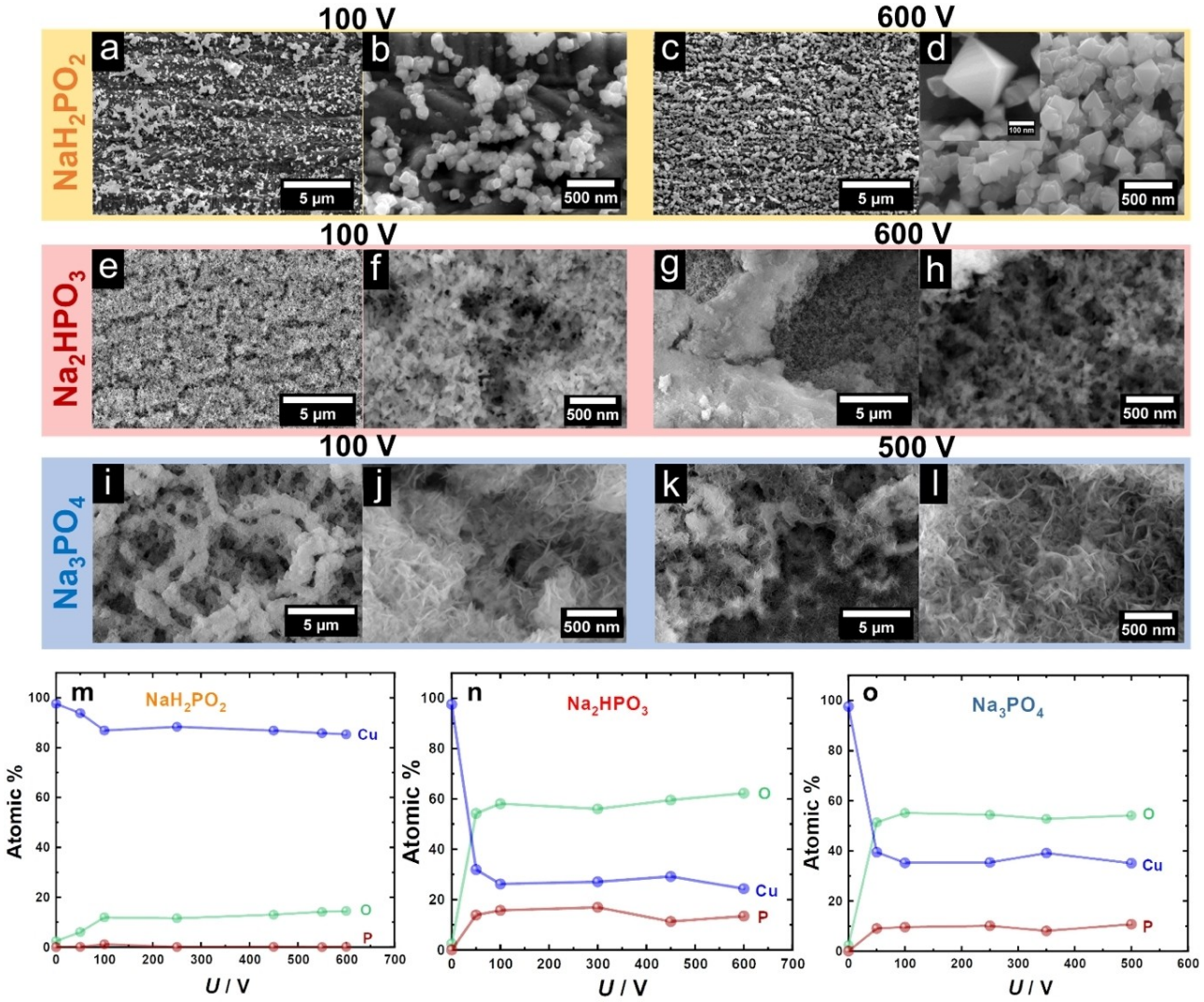

Figure 2. Changes in the surface morphology and chemical composition of Cu electrodes after electrolysis as a function of electrolyte and applied voltage. SEM micrographs of Cu electrodes after electrolysis for 15 s in NaH_2PO_2 (a–d), Na_2HPO_3 (e–h), and Na_3PO_4 (i–l) electrolyte at different voltages. EDS elemental compositions Cu electrodes after electrolysis for 15 s in NaH_2PO_2 (m), Na_2HPO_3 (n), and Na_3PO_4 (o) electrolyte as a function of the applied voltage. Solid lines are for the visual representation of the data.

this, the Cu dissolution is more noticeable after polarization in NaH_2PO_2 and Na_2HPO_3 than in Na_3PO_4 and at the applied voltages that generate higher electric current during electrolysis (see the *I–U* behavior, Figure 1). Figures 2a–l and Figures S3–S5 demonstrate that the identity of the electrolyte anions determines the final surface morphology of the polarized Cu electrodes. Polarizing the Cu surfaces generates octahedral nanocrystals using NaH_2PO_2, a nano-porous structure using Na_2HPO_3, and a macro-porous structure using Na_3PO_4. After polarization in 0.1 M NaH_2PO_2 at 100 V (normal electrolysis regime), octahedral nanoparticles (particle size: 50–100 nm) with shape imperfections are formed (Figures 2a and 2b). Notably, the shape of these octahedral nanocrystals gets more and more well-defined, and their density increases with a further increase of the applied voltage (Figure S3a). After plasma electrolysis at 600 V, the octahedral nanocrystals are well-defined, larger (around 200–300 nm), and homogenously distributed over the Cu surface (Figures 2c and 2d). The formation of Cu octahedral nanocrystals might be due to the reduction of CuO as supported by X-ray photoelectron spectroscopy (XPS), which will be illustrated later. Furthermore, it seems that as the applied voltage increases, the temperature increases leading to the formation of more and more nuclei, some of which are rapidly cooled and combined to form octahedral nanoparticles by an aggregation growth mechanism.[48] The shape of metal nanoparticles is typically determined by the rate at which they form, known as "kinetic control".[49] Nanoparticles with octahedral shapes are anticipated for slower growth rates, however, more complex shapes, which contain more edges and have lower symmetry are expected for faster growth. The observed shapes in this study, following polarization in NaH_2PO_2, align well with the expectations for slow-growth-rate particles, indicating that the growth process is primarily influenced by kinetic control.

The surface of the Cu electrode treated in Na_2HPO_3 at 100 V is entirely covered with a high density of nano-porous structures, as shown in Figures 2e and 2f. Identical nano-architectures are observed even at higher voltages up to 450 V (Figure S4). Interestingly, plasma electrolysis at 600 V results in much rougher Cu surfaces characterized by the formation of multi-layers of the nano-porous structures with increased porosity, as demonstrated in Figures 2g and 2 h.

Anodic polarization in 0.01 M Na_3PO_4 at 100 V and 250 V induces the formation of homogenously distributed micro-porous patterns on the surface of the Cu electrodes (Figures 2i, 2j, and S5). The micro-porous pattern becomes ill-defined with further increase of the applied voltages up to the plasma electrolysis regime ($400\ V \leq U \leq 500\ V$), as shown in Figure S5 and Figures 2k and 2l. This behavior can be attributed to the increase in local temperature at the electrode surface. Higher SEM resolution reveals that the Cu surface consists of smaller nano petals after plasma electrolysis at 500 V (Figure 2l). The formation of nano-porous and micro-porous structures after polarization in Na_2HPO_3 and Na_3PO_4, respectively, points towards Cu dissolution during electrolysis. Furthermore, the evolution of huge amounts of gas bubbles and the incorporation of P into the Cu surface affect the final surface morphology.[35]

Figures 2m–o illustrate changes in the elemental composition of the Cu electrodes monitored by energy dispersive spectroscopy (EDS) analysis upon polarization in the employed electrolytes at different voltages. Polarization of Cu electrodes leads to an increase in the fraction of atomic O. After polarization in NaH_2PO_2, a tiny amount of P (< 1 %) is detected, while the O content increases as a function of the applied voltage reaching its maximum of around 14 % at 600 V. Atomic O is uniformly distributed over the surface of the octahedral nanocrystals as indicated by EDS elemental mapping (Figure S6a). In comparison, the nano-porous and micro-porous structures contain a much higher content of O (62.3 % for Na_2HPO_3 and 55.1 % for Na_3PO_4) and P (13.5 % for Na_2HPO_3 and 11.0 % for Na_3PO_4) after plasma electrolysis. These values are comparable to those obtained after polarization at different voltages (Figures 2m–o). Notably, O and P are homogenously distributed through the entire nano-porous and micro-porous structures, as shown in Figures S6b and 6c. These results reveal the incorporation of P atoms into the Cu electrodes, particularly after electrolysis in Na_2HPO_3 and Na_3PO_4. To put it in a simple way, hypophosphite, phosphite, and phosphate anions can undergo disproportionation during anodic polarization at the electrode/electrolyte interface under the action of electric current.[50] This generates P, which can diffuse into a metallic Cu lattice during polarization in Na_2HPO_3 and Na_3PO_4 solutions. The diffusion of P into the Cu lattice explains the appearance of the XP signal associated with metallic P (Figure S7b,c). The P atoms might preferentially substitute some of the Cu atoms rather than occupy the spaces between them.[31] As a result, this incorporation of P into Cu triggers the formation of a porous surface.

XPS analysis was performed to identify alterations in the chemical composition and oxidation state of Cu species of the topmost oxide layer after plasma treatment for 15 s in 0.01 M NaH_2PO_2, Na_2HPO_3, and Na_3PO_4 at 600 V, 600 V, and 500 V, respectively. Moreover, XPS depth profiling measurements were conducted with various sputter depth rates of 3, 10, and 30 $nm \cdot min^{-1}$ to probe the subsurface chemical states of Cu.

Figures 3a–d compare the deconvolution of the Cu $2p_{3/2}$ signal in the XP spectra for both the as-polished and plasma-treated Cu electrodes. The Cu $2p_{3/2}$ binding energy (BE) is 934.7 eV for $Cu(OH)_2$, 933.6 eV for CuO, and 932.3 eV for Cu_2O or metallic Cu.[51–53] Metallic Cu (932.2–932.7 eV) and Cu_2O (932.0–932.6 eV) have an overlapping Cu $2p_{3/2}$ BE range. Hence, it is unfeasible to discriminate Cu and Cu_2O with the Cu $2p_{3/2}$ signal. According to the obtained spectrum in Figure 3a, the as-polished Cu electrode is composed of CuO and Cu_2O/Cu(0). Notably, after polarization in NaH_2PO_2, the intensity of the CuO peak significantly reduces and the main surface composition of the Cu electrode is Cu_2O/metallic Cu (Figure 3b). Seemingly, Cu_2O is present on the surface since EDS-mapping reveals that O is uniformly distributed on the surface of the octahedral nanocrystals (see Figures 2m and S6a). The subsurface chemical states of Cu are similar, as revealed by the XP spectra obtained at different depth rates. In comparison, the top surface of the

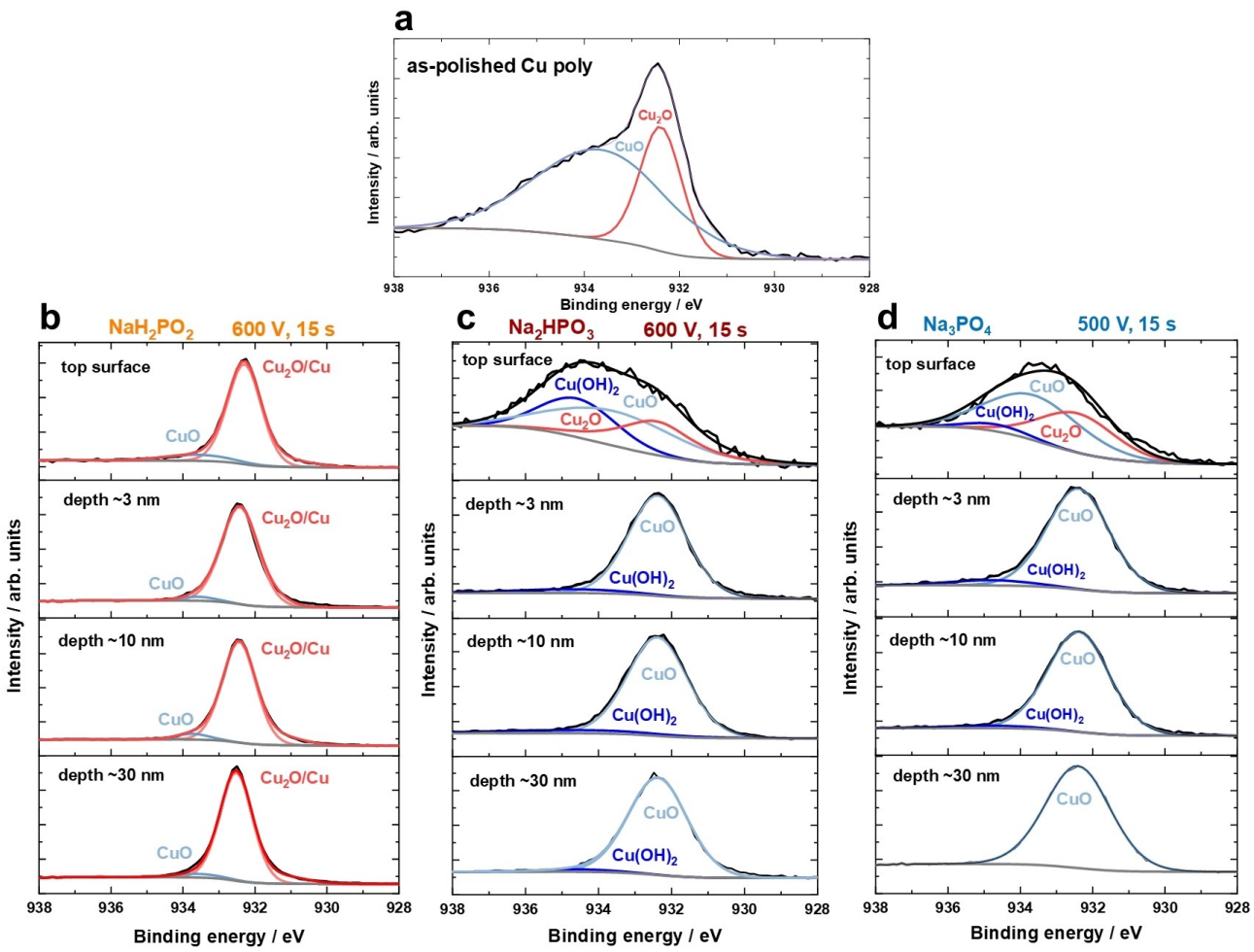

Figure 3. Materials characterization. X-ray photoelectron spectra of core level Cu 2p of the as-polished Cu electrode (a), and after plasma treatment for 15 s in NaH_2PO_2 at 600 V (b), Na_2HPO_3 at 600 V (c), and Na_3PO_4 at 500 V (o). Depth profiling spectra of plasma modified Cu electrode recorded at about 3, 10, and 30 nm·min^{-1} Ar^+ sputtering. The spectra are fitted with a linear combination of the corresponding Cu, Cu_2O, and CuO reference spectra.

Cu after plasma treatment in Na_2HPO_3, and Na_3PO_4 is composed of Cu_2O, CuO, and $Cu(OH)_2$ (see Figures 3c and 3d). The appearance of $Cu(OH)_2$ on the surface is attributed to OH adsorption on different low-index surfaces during plasma electrolysis in alkaline media. Furthermore, the XPS depth profile analysis shows that the subsurface of Cu is composed of a significant amount of CuO and a negligible amount of $Cu(OH)_2$.

The broad P 2p high-resolution spectra are deconvoluted in three P $2p_{3/2}$–P $2p_{1/2}$ doublets that correspond to PO_4^{3-} at ≈132.2 eV, PO_3^{2-} at ≈133.2 eV and PO_2^- at ≈134.4 eV (Figure S7).[54] The presence of P–O species, resulting from surface oxidation during plasma electrolysis, indicates the successful P incorporation into surface and subsurface sites of Cu by plasma electrolysis in the employed electrolytes.

Electrochemical characterization

The structural changes of the Cu electrodes induced by the anodic polarization in 0.01 M NaH_2PO_2, 0.01 M Na_2HPO_3, and 0.01 M Na_3PO_4 for 15 s as a function of the applied voltage were monitored using cyclic voltammetry. Figures 4a–d compare the first cycle of the cyclic voltammetric profiles in 0.1 M KOH at a scan rate of $s = 50\ mV\,s^{-1}$ for as-polished and modified Cu electrodes. The first cycles were measured after holding the potential at −0.2 V vs. RHE until the Cu oxides reduction current was in the range of 400 nA. Moreover, the current in these voltammetric profiles is normalized to the electrochemically active surface area (EASA). The EASA has been estimated by equating the double-layer capacity of the anodically polarized and as-polished Cu electrodes at −0.10 V vs. RHE, where neither Faraday reactions nor adsorption processes occur.[30,55–57] Generally, for Cu electrodes, the peaks observed in the regime between 0.2 V and 0.4 V vs. RHE can be ascribed to the formation and reduction of Cu_2O.[58] The peaks at potentials below 0.2 V can be attributed to OH adsorption and desorption on different low-index surface facets.[59,60] After electrolysis, the Cu surface shows several (distinct) peaks between 0.25 and 0.40 V, whose individual current densities differ as a function of the anions of the P-based electrolytes, indicating that such treatment results in surfaces having a modified (preferential)

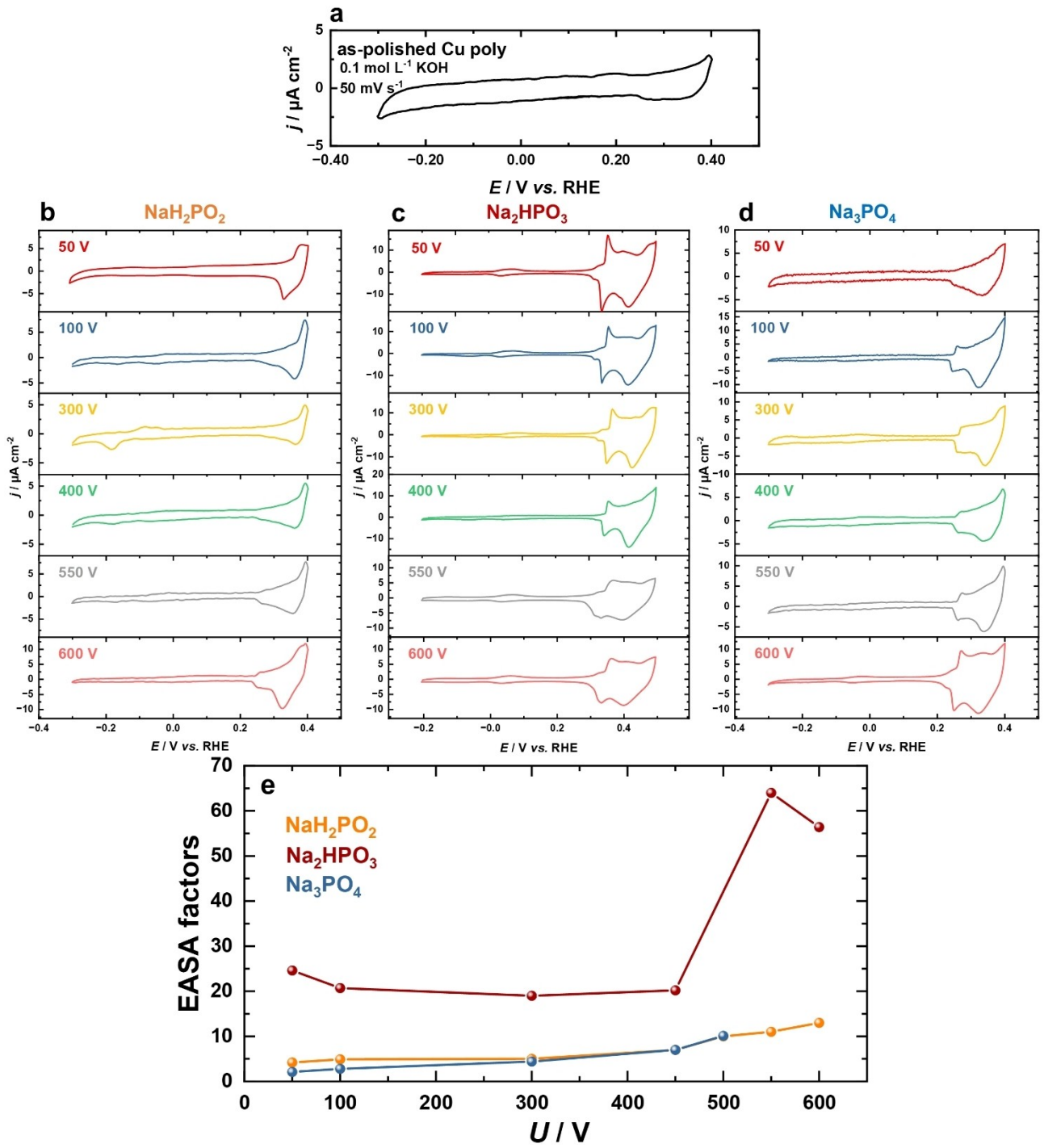

Figure 4. Electrochemical characterization. Cyclic voltammetry profiles of Cu electrodes in 0.1 M KOH at 50 mV s^{-1} before (a) and after anodic polarization in 0.01 M NaH_2PO_2 (b), Na_2HPO_3 (c), and Na_3PO_4 (d) electrolytes at different applied voltages for 15 s. e) The corresponding electrochemically active surface area factors as a function of applied voltages. Solid lines in (e) are for the visual representation of the data.

facet distribution compared to the starting surface (see Figures 4a–d).

From a structure and symmetry point of view, the octahedral nanocrystals are indicative of a (111)-surface.[43,61] The anodic peak at around 0.01 V and the cathodic peak at about −0.09 V vs. RHE, related to the adsorption and desorption of OH on Cu(111) terraces, reveal that the anodic polarization in $Na_2H_2PO_2$ generates Cu(111) facets (Figure 4b). On the other hand, the absence of (111)-features in some of the voltammograms (Figure 4b) might result from the formation of small (111) terraces and the high ratio of step-to-terrace sites.[60] The current-potential profiles of Cu electrodes polarized in Na_2HPO_3 and Na_3PO_4 show fingerprints comparable to those known for Cu(111)-surfaces. Besides, the peaks of low intensity at about

0.08 V vs. RHE are related to the adsorption and desorption of OH on Cu(110) terraces, revealing the formation of Cu(110) sites upon anodic polarization in Na_2HPO_3 and Na_3PO_4 (Figures 4c and 4d).[59,60,62] Figure 4e shows changes in the EASA factors after polarization in the employed electrolytes at several applied voltages compared to the pristine Cu electrode. Notably, the Cu electrodes treated in NaH_2PO_2 and Na_3PO_4 show comparable EASA values at different applied voltages. The EASA factors enhance with increasing the applied voltages, reaching a maximum of about 10 times in the plasma electrolysis regime. In comparison, polarization in Na_2HPO_3 results in an extraordinary increase of the EASA over the whole applied voltages. The EASA factors are in the range of 19–25 after polarization with $50\,V \leq U \leq 450\,V$. Fascinatingly, plasma electrolysis in Na_2HPO_3 at 550 V massively increases the EASA by a factor of 65 compared to the pristine Cu surface. During electrolysis of the employed electrolytes under relatively high applied voltages ($U \geq 50$ V) the Cu surface is supposed to become rather brittle (large surface stress) and partial decomposition (dissolution) appears to increase the surface to extenuate the constraint. The trends obtained for the EASA factors are in line with the SEM observations (see Figures 2 and 4e). The SEM micrographs exhibit that the polarization of Cu electrodes in NaH_2PO_2 generates a high density of nano-porous structures. Accordingly, the EASA increases, especially after plasma electrolysis due to the formation of multi-layers of these structures with increased porosity. Furthermore, the Cu electrodes with nano-porous structures are expected to have higher EASA compared to those with octahedral nanocrystals and micro-porous structures.

CO_2 electroreduction reaction (CO_2RR)

The (electro)catalytic performance for the CO_2RR can be significantly affected by the morphology of Cu, whether it is in the form of planar electrodes or nanoparticles.[13,63–65] In a recent study by Jiang et al.,[9] the effect of a gas-phase plasma using Ar, O_2, and N_2 on the surface roughness of Cu was investigated, and its relationship with selectivity was emphasized. In our study, we further explore the role of surface structure (surface morphology and roughness) and the effect of phosphorous incorporation on the electrocatalytic performance of Cu electrodes towards CO_2RR. To fabricate the electrocatalysts, planar Cu foils were anodically polarized in 0.01 M solutions of NaH_2PO_2, Na_2HPO_3, and Na_3PO_4 at 600, 600, and 500 V, respectively. The surface morphology and EDS elemental composition of the plasma-treated Cu foils closely resemble those observed for Cu wires under similar experimental conditions (Figures 2 and S8). The as-polished Cu electrode was used as a reference for comparison, as previously described.[66] Planar electrodes were chosen for their homogeneous electrical field distribution and simple geometrical area, facilitating comparison with other electrode shapes.

To efficiently assess the electrocatalytic performance of the modified Cu electrocatalysts towards CO_2RR across a range of potentials, we employed "electrochemical real-time mass spectrometry",[67] a technique that allows for the real-time detection of reaction products during an electrochemical experiment using a mass spectrometer. Linear sweep voltammetry was conducted to evaluate the production of ethylene, an industry-relevant CO_2RR product, and hydrogen, a common byproduct in aqueous electrolytes, as illustrated in Figure 5a. The results show that Na_3PO_4 exhibits the highest selectivity for ethylene, whereas Na_2HPO_3 yields the most hydrogen. Furthermore, the onset potential of ethylene formation for the modified electrocatalysts was determined. This onset is defined as the potential where the signal of the ethylene product is twice as high as the fluctuations. The ethylene onset potentials for the Cu electrodes polarized in Na_2HPO_3 and Na_3PO_4 are −0.57 and −0.61 V vs. RHE, respectively. These values were notably less negative than that of the as-polished Cu electrode, which is around −0.72 V vs. RHE, and are represented by the dashed line in Figure 5a. Similar to oxide-derived copper, the modified catalysts displayed a significant effect in shifting the ethylene onset potential, up to 0.2 V.[68] It is important to note that as the modified electrocatalysts do not have identical EASAs, the scan over the potential region provided only qualitative information.

Chronoamperometric measurements were performed at −1.1 V vs. RHE to qualitatively compare the performance of plasma-modified electrocatalysts and as-polished Cu, with a focus on the selectivity towards ethylene and other C_2 products. This potential has been reported in the literature as being the most selective for ethylene and most C_2 products in the case of as-polished Cu electrodes.[66,69] The faradaic efficiencies for ethylene and hydrogen are plotted in Figure 5b, which corroborated the trends observed during real-time analysis. The EASA of these plasma-modified Cu foils is determined by comparing capacitances in a non-faradaic potential region, as shown in Figure S9. Notably, the EASA values of these Cu electrodes are comparable to those obtained for the Cu wires (Figure 4e and Figure 5c). The roughness of the modified Cu electrocatalysts, which is directly proportional to the EASA, increased by factors of 16.3, 63.1, and 10.3 after plasma electrolysis in NaH_2PO_2, Na_2HPO_3, and Na_3PO_4, respectively, compared to the as-polished Cu electrode. This increase in EASA is reflected in the total current recorded in the experiments shown in Figure 5c, where the total geometrical current density increased up to 89 $mA\,cm^{-2}_{geo}$ for Na_2HPO_3 compared to 16.5 $mA\,cm^{-2}_{geo}$ for as-polished Cu electrodes. Figure 5c displays the total current density for the geometrical CO_2RR, whereas Figure S10 presents the partial current density for each product. Only the electrode treated in NaH_2PO_2 shows similar or lower CO_2RR partial current densities than the as-polished Cu electrode. Overall, the described plasma treatment could potentially increase the geometrical current for CO_2RR by a factor of approximately three.

After plasma electrolysis in Na_3PO_4, the Cu electrode exhibits noteworthy selectivity towards C_2 products. Specifically, the electrode produces ethylene, ethanol, and acetaldehyde at rates of 23, 7, and 14%, respectively. This Faradaic efficiency increase may be attributed to several factors. Firstly, the incorporation of phosphorus into the Cu surface, as demon-

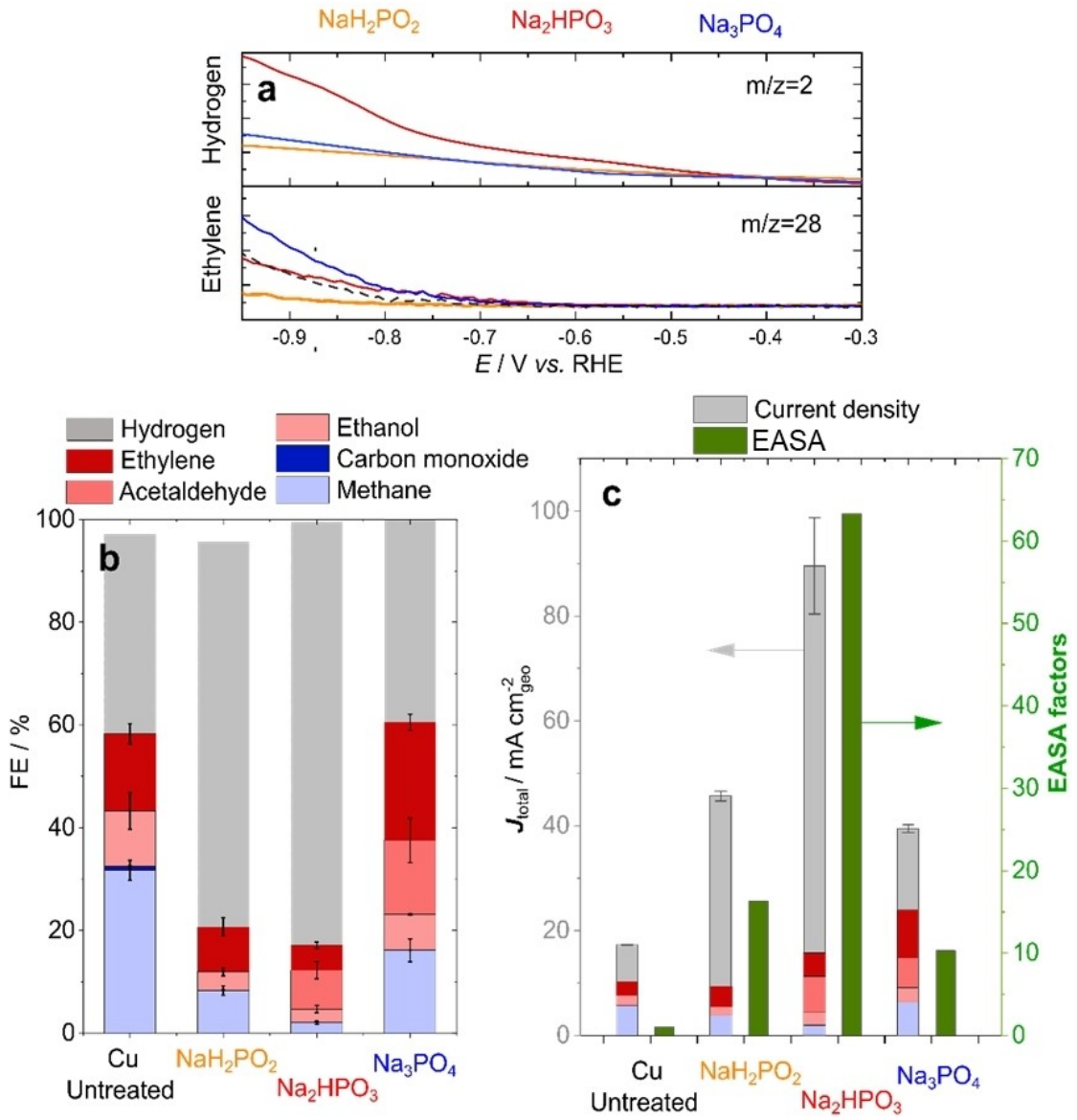

Figure 5. a) Mass-intensity signal of hydrogen and ethylene during linear sweep voltammetry experiments conducted at a scan rate of 15 mV s^{-1} using a 0.1 M potassium hydrogen carbonate saturated with CO_2 (pH 6.8) electrolyte. b) Faradaic efficiencies for CO_2RR and water splitting are determined at −1.1 V vs. RHE using as-polished Cu and plasma-modified Cu electrodes as working electrodes. Electrolysis time was 60 minutes. c) Total current for the experiments is presented on the left *y*-axis, whereas the EASA relative to the geometrical surface of the corresponding plasma-treated electrode is shown on the right *y*-axis.

strated by EDS and XPS analyses, may alter the electronic state of neighboring Cu atoms due to its high electronegativity. Recent theoretical calculations have attributed the high selectivity towards C_2 products in phosphorous-doped Cu electrodes to the presence of adsorbed *COCOH, an intermediate whose stabilization is often used as a descriptor for generating C_2 products.[70,71] Furthermore, the distribution of the Cu facets after polarization in Na_2HPO_3 and Na_3PO_4 (Figure 4) shows the existence of Cu(110) facets, which require less energy to stabilize *COCOH compared to Cu(111). This stabilization is even more favorable on rough surfaces, such as those of the modified electrocatalysts, particularly at grain boundaries.[71,72] Additionally, the high roughness of the modified catalysts results in a substantial variation of the pH close to the electrode surface due to the generation rate of OH^-. It is known that an increased pH enhances the ratio between ethylene and methane production.[69] The macro-porous structure of this electrode may also contribute to its high selectivity towards C_2 products, as it provides enhanced CO_2 transport, enabling it to maintain high CO_2RR selectivity for C_2 products even at relatively large geometrical current densities of 38 mA·cm^{-2}_{geo}. In contrast, the Cu electrode polarized in Na_2HPO_3 exhibits lower CO_2RR selectivity towards C_2 products which might be due to its extremely large EASA leading to mass-transport limitation of CO_2. Therefore, further investigations were performed for CO_2RR at different potentials lower than −1.1 V vs. RHE, as will be discussed below.

Notably, the Cu electrodes polarized in Na_2HPO_3 and Na_3PO_4 produce significantly more acetaldehyde compared to the as-polished Cu electrode, which has a Faradaic Efficiency (FE) lower than 1%. The production of acetaldehyde is highly dependent on the crystallography of Cu and is favored by the presence of Cu(110).[73] The highest recorded FE for acetaldehyde production is 25% for Cu(110) single crystals.[74] While the selective production of acetaldehyde is rarely studied, recent research has shown that doping Ag atoms into a Cu lattice can increase the selectivity of CO electroreduction towards acetaldehyde at relatively low potentials.[75] Similarly, phosphorous incorporation and the presence of rich Cu(110) can have a similar effect by increasing the energy of the crucial intermediate CH_3CH_2O and hindering the transformation of acetaldehyde to ethanol.

The Cu electrodes polarized in Na_2HPO_3 and NaH_2PO_2 exhibit a noteworthy prevalence of the hydrogen evolution reaction, with rates exceeding 80%. To explain this, the Cu electrode polarized in NaH_2PO_2 possesses octahedral nanostructures that are rich in Cu(111) facets, which are known to be more active for hydrogen evolution than for CO_2RR.[73,76]

To explore possible practical applications for plasma-modified electrocatalysts, additional experiments were conducted using 0.5 M $KHCO_3$ as an electrolyte at −0.75 and −0.95 V vs. RHE, as depicted in Figure S11. The choice of higher electrolyte concentrations was motivated in order to avoid changes in the bulk pH value, especially for such rough Cu electrodes. Since CO_2 is barely soluble in alkaline media and readily transforms to carbonate in water, this change in concentration is necessary. Interestingly, the results in Figure 6 indicate that the Cu electrode polarized in Na_2HPO_3 demonstrated the highest faradaic efficiencies towards C_2 and C_3 products at −0.75 and −0.95 V vs. RHE, with 7.5% efficiency towards 1-propanol. This observation suggests an early onset potential for oxygenates, which is further supported by the demonstration of the earliest onset potential to ethylene (−0.57 vs. RHE) among all the modified electrocatalysts.

The favorable adsorption of CO on the modified electrocatalysts, as indicated by their surface roughness and CO binding energy, diminishes the release of CO and promotes C–C bonding,[9,19] as shown in Figures 6a and 6b. This relationship is further illustrated in Figure 6b, which displays a linear correlation between roughness and the ratio of C_3 (1-propanol) to C_1 (formate and CO) faradaic efficiencies. The slope of this correlation decreases with increasing overpotential, which we attribute to the mass transport limitation of CO_2. This limitation is also suggested by the flattening of the CO_2RR partial current density, as seen in Figure S12.

Table S1 presents a comparison between our results for the fabricated Cu electrodes using in-liquid plasma and those reported in previous studies, including Cu electrodes prepared through gas-phase plasma.[9,20,38,77–80] Compared to previously reported Cu electrodes fabricated by different methods (Table S1), the Cu electrodes prepared through in-liquid plasma treatment in Na_3PO_4 exhibit higher total geometrical activity, outperforming most of the reported studies and demonstrating significant production of C_2 products. Additionally, both Cu electrodes treated in Na_2HPO_3 and Na_3PO_4 produce acetaldehyde, a unique observation compared to these reported Cu electrocatalysts. It is essential to consider that variations in sample preparation and investigative conditions may pose challenges in making direct and precise comparisons between different studies. Nevertheless, our study demonstrates the capabilities of in-liquid plasma electrolysis to fabricate diverse micro/nano-structured and porous Cu electrodes, which are of special interest for CO_2RR applications. Moreover, it advances our understanding of CO_2 electroreduction at Cu electrodes modified by in-liquid plasma electrolysis in different phosphorus-oxoanion-based electrolytes, serving as a launching point for further investigations in this area.

One of the primary challenges in CO_2 electrolysis lies in ensuring the long-term stability of the electrode's electrocatalytic performance. Cu electrocatalysts typically undergo surface structural changes during CO_2RR operation conditions, leading to variations in activity and selectivity over time.[1,81] To address this issue, we conducted 10-hour electrolysis experi-

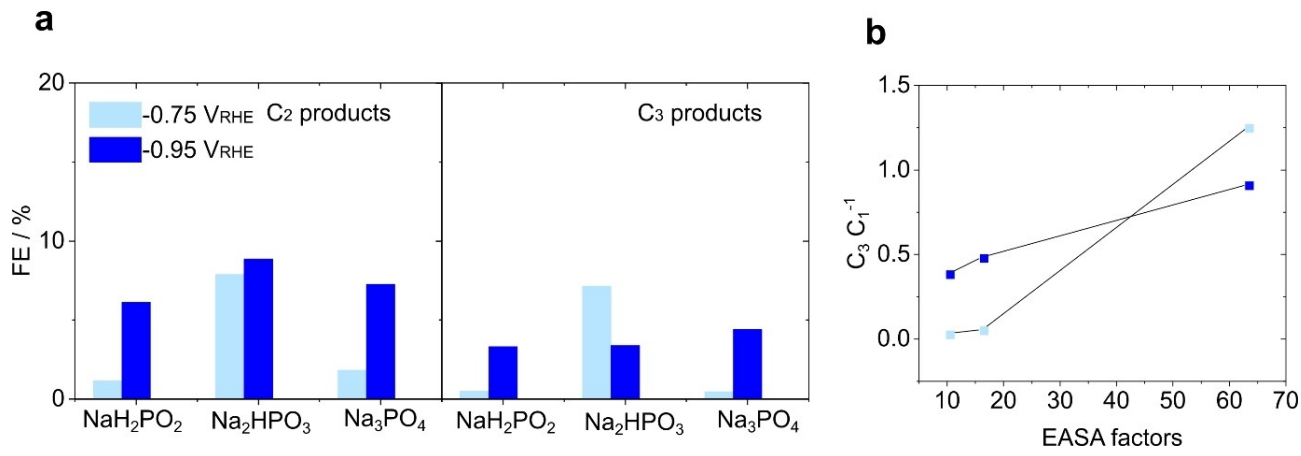

Figure 6. a) Sum of the Faradaic efficiencies for CO_2RR products with two and three carbon atoms presented separately and the ratio of C_3/C_1 products (b) as a function of the electrochemically active surface area for plasma-modified Cu electrodes. The electrolyte used was 0.5 M potassium hydrogen carbonate saturated with CO_2 (pH 6.8), and the electrolysis time was 60 minutes.

ments at −1.1 V vs. RHE, as displayed in Figure S13. The Cu electrodes prepared through plasma electrolysis in NaH_2PO_2 and Na_3PO_4 displayed similar behavior, with the total current density increasing steadily for the first 90 minutes and then stabilizing for about 7.5 hours for NaH_2PO_2 and at least 10 hours for Na_3PO_4. However, for the Cu electrode treated in NaH_2PO_2, the total current density gradually decreased after 7.5 hours, resulting in a 20% loss of activity after 10 hours. The initial rise in current density may be attributed to surface structural changes in the Cu electrodes, as indicated by the SEM images (Figure S14 and Figure S15). During the first hour of electrolysis, hydrogen production increased by 20% and 10% for Cu electrodes treated in NaH_2PO_2 and Na_3PO_4, respectively, which correlates with the rise in total current density. Additionally, the ethylene faradaic efficiency of the Cu electrode treated in Na_3PO_4 decreased from 25% to 18% after 10 hours, possibly due to arising impurities from the electrolyte.[81]

Furthermore, we monitored the surface morphology of plasma-modified Cu electrodes after 1 hour and 10 hours of CO_2RR at −1.1 V vs. RHE (Figure S14a–f and Figure S15a–f). Remarkably, structural transformations are observed in Cu electrodes polarized in NaH_2PO_2, Na_2HPO_3, and Na_3PO_4 electrolytes after CO_2RR (Figure 2, Figure S14, and Figure S15). After 1 hour of CO_2RR, the surface of Cu octahedral nanocrystals shows increased roughness, possibly due to dissolution under highly reducing conditions (Figures S14a and S14b). The enhanced roughness during CO_2RR could be one of the factors contributing to the initial rise in total current density during the first hour of electrolysis. In comparison, Cu electrodes polarized in Na_2HPO_3 and Na_3PO_4 exhibit surface restructuring, forming nanoparticle clusters that assembled into porous patterns (Figures S14c–f). The nanoparticle clusters formed in Na_2HPO_3 are smaller and arranged in a nanoporous pattern (Figures S14c and S14d), whereas in Na_3PO_4, they formed microporous patterns (Figures S14e and S14f). These structural transformations likely occur at the early stages of CO_2RR, resulting from the reduction of the oxide layer formed during plasma electrolysis. Notably, the Cu electrode prepared in NaH_2PO_2 shows noticeable changes, with octahedral nanocrystals becoming more agglomerated and ill-defined after 10 hours of CO_2RR (Figure S15a–c). In comparison, the surface morphology of the Cu electrode polarized in Na_3PO_4 after 10 hours of CO_2RR reveals the presence of pit cavities (Figure S15d–f). These pit cavities indicate surface restructuring and corrosion processes occurring during CO_2RR. Given the critical importance of stability, a comprehensive investigation into such structural transformations and their impact on electrocatalytic performance will be the focus of a subsequent and extensive study.

Conclusions

In this study, we investigated the evolution of surface structure and composition of Cu electrodes after anodic polarization in three different P-based electrolytes, including NaH_2PO_2, Na_2HPO_3, and Na_3PO_4 at a wide voltage regime ranging from 50 up to 600 V. The nature of the electrolyte anions plays a crucial role in the *I–U* characteristics, electrochemical behavior, electrochemically active surface area (EASA), as well as final surface morphology and composition of the polarized Cu electrodes. Polarizing the Cu surfaces in NaH_2PO_2 generates octahedral nanocrystals, whereas in Na_2HPO_3 it results in a nano-porous structure, and Na_3PO_4 produces a macro-porous structure. The energy dispersive spectroscopy (EDS) and X-ray photoelectron spectroscopy (XPS) analyses reveal the incorporation of P into the polarized Cu surfaces, especially for those with nano- and micro-pores. Moreover, the electrochemical characterizations demonstrate that the electrolysis results in Cu surfaces with modified facet distribution and the formation of Cu(111) in the case of octahedral nanocrystals and Cu(110) sites for the nano-porous and micro-porous structures. The EASA factors increase with increasing the applied voltages, with the highest increase observed for Cu electrodes polarized in Na_2HPO_3, which is in line with the formed nanostructures. We also evaluated the electrocatalytic activity of the plasma-treated Cu electrodes, characterized by the presence of P and different roughness, surface morphology, and facets, towards electrochemical reduction of CO_2 (CO_2RR). Plasma treatment leads to a higher geometrical current for CO_2RR due to the significant increase in the surface roughness of the Cu electrodes. Interestingly, the Cu electrode polarized in Na_3PO_4 exhibits noteworthy selectivity towards C_2 products, including ethylene, ethanol, and acetaldehyde, at −1.1 V vs. RHE. This selectivity increase is attributed to the incorporation of phosphorus and the existence of Cu(110) facets, which are more favorable for *COCOH stabilization than Cu(111) facets. The incorporation of phosphorus into the Cu surface might alter the electronic state of neighboring Cu atoms and promote the stabilization of intermediate species involved in the formation of C_2 products. On the other hand, the Cu electrodes polarized in Na_2HPO_3 and NaH_2PO_2 exhibit a remarkable prevalence of the hydrogen evolution reaction, with rates exceeding 80% at −1.1 V vs. RHE. The low selectivity of the Cu electrode polarized in Na_2HPO_3 could be explained by its extremely large EASA resulting in mass-transport limitation of CO_2 at −1.1 V vs. RHE. The observed abundance of Cu(111)-facets after polarization in Na_2HPO_2, given that the electrode surface is composed of octahedral particles, appears to favor hydrogen evolution, despite having a smaller EASA compared to Na_2HPO_3. The CO_2RR investigations at lower potentials (−0.75 and −0.95 V vs. RHE) indicate that the Cu electrode polarized in Na_2HPO_3 has the highest faradaic efficiencies towards C_2 and C_3 products, with an early onset potential for oxygenates, particularly 1-propanol. These findings establish a solid foundation for the development of Cu electrodes with optimized surface structures, thereby enhancing their efficiency in a wide range of energy applications. Moreover, this study advances the fundamental understanding of CO_2 electroreduction at Cu electrodes that have been modified through in-liquid plasma electrolysis using various phosphorus-oxoanion-based electrolytes. Essentially, we show the potential for plasma-modified Cu electrocatalysts to contribute to sustainable CO_2 reduction and carbon capture technologies.

Experimental Section

Plasma experiments

The electrolytes were prepared using ultra-pure water (18.2 MΩ cm, TOC ≤ 3 ppb), and all chemicals were used without further purification. To perform plasma electrolysis (PE), a TDK-Lambda programmable DC power supply (GEN600-1.3/E, 1 U, 780 W, RS-232/RS-485) was used, with the LabVIEW software (National Instruments) to control the power supply and record voltage and current data. The PE was carried out in a 300 mL double-walled glass cell with magnetic stirring and a water-cooling system to maintain the electrolyte temperature at about 30 °C. The working electrode (anode) was a 0.05 mm thickness Cu sheet or a 0.5 mm diameter Cu wire (99.995 + %, MaTecK, Jülich, Germany), whereas the counter electrode (cathode) was made of stainless steel with dimensions of 20 mm×20 mm×2 mm. To remove organic contaminants and the native oxide layer from the Cu surface, it was sonicated in 85 % phosphoric acid (Merck) for 60 seconds and rinsed thoroughly with ultra-pure water before use. Polypropylene tips were used on both sides of the Cu wire to define the treatment area and ensure a uniform electric field during electrolysis. The cathode and anode were kept at a distance of 50 mm. The Cu electrodes were polarized in 0.01 M of sodium hypophosphite ($NaH_2PO_2 \cdot H_2O$, ≥ 98 %), disodium hydrogen phosphite (Na_2HPO_3, ≥ 98 %), or trisodium phosphate (Na_3PO_4, ≥ 99.999 %). After the experiment, the prepared electrodes were rinsed thoroughly with ultra-pure water and dried in a flow of N_2 gas.

Characterization

The Cu electrodes were analyzed using scanning electron microscopy (FIB-SEM) coupled with energy dispersive spectroscopy (EDS) to determine their surface morphologies, chemical composition, and elemental mapping. Imaging was performed at an accelerated voltage of 10 kV. The chemical composition, oxidation states, and depth profiling of the Cu surfaces were analyzed using X-ray photoelectron spectroscopy (XPS) measurements with monochromatized Al K_α (1486.6 eV) radiation and a detection angle of 45°. For depth profiling XPS measurements, a successive Argon ion (Ar^+) sputter treatment was carried out. The topmost surface layers were removed using Ar^+ sputtering ($I_{sp} \approx 1$ mA; $U_{sp} = 5$ kV) with ca. 1, 3, and 30 nm min^{-1}. To neutralize the surface charge, a low-energy electron flood gun (current, 3 μA) was used to deliver electrons to the sample surface. All binding energies were calibrated from the main carbon peak using the C 1s peak at 284.8 eV. Electrochemical measurements were conducted in a conventional three-electrode glass cell using an Autolab PGSTAT128 N potentiostat with a Scan250 module. The HydroFlex RHE electrode (Gaskatel) served as the reference electrode, and a graphite rod was utilized as the counter electrode for the characterization of the electrodes in 0.1 M KOH electrolyte. Nitrogen was used to deaerate the electrolyte before and during the experiments. All electrochemical measurements were performed at room temperature (19–22 °C).

CO_2 electroreduction reaction

The steady-state electrolysis experiments were conducted in a two-compartment PTFE electrolysis cell, which was separated by a bipolar membrane (Fumasep). To form a three-electrode setup, Ag/AgCl (BASi), Ir-MMO (Metakem), and Cu electrodes restricted to 1.0 cm^2 were used as reference, counter, and working electrodes, respectively. The $KHCO_3$ (99.997 + %, Puratronic, Alfa Aesar) electrolyte was continuously saturated with 20 sccm CO_2 using an EL-flow prestige (Bronkhorst) mass flow controller. Before each experiment, all Cu oxide was reduced through linear sweep voltammetry from open circuit potential to −1.8 V with a scan rate of 50 mV s^{-1}. The hour-long experiments, which were repeated at least twice per potential and electrocatalyst, were controlled by a Reference [600] Gamry potentiostat. Electrochemical impedance spectroscopy was performed before and after the chronopotentiostatic experiments to correct the *IR*-drop during the electrolysis using the positive feedback mode of the potentiostat. To ensure comparability, the potentials measured in Ag/AgCl were transformed to RHE, taking into account the neutral pH of the saturated electrolyte.

Product analysis

The gas and liquid products were quantified separately. The gaseous stream of CO_2 was analyzed by an online gas chromatograph (GC) system (Clarus 580 – Arnel Engineered, Perkin Elmer) that consisted of two chromatography columns – a Hayesep N (NR021501, Perkin Elmer) and a Molecular Sieve 13X (NR022501, Perkin Elmer). The products' signal was obtained in parallel using a thermal conductivity and a flame ionization detector that was calibrated with a 1000 ppm gas mixture of each gas (Air Liquide). Methane, ethylene, carbon monoxide, and hydrogen were detected by the system. Faradaic efficiencies were calculated using an average concentration value from four time-equidistant injections.

The volatile liquid products were analyzed using gas chromatography-mass spectrometry (GC-MS) (Clarus 580 coupled to Clarus SQ8T, both Perkin Elmer), which was coupled with a headspace autosampler (Perkin Elmer TurboMatrix 40). The samples extracted from the vapor phase of a heated vial were passed through a fused silica capillary column (Elite-624Sil MS, Perkin Elmer) to separate the products, and were detected using electron ionization (70 eV) and a quadrupole mass analyzer.

Electrochemical real-time mass spectrometry (EC-RTMS)

The electrolyte was passed through a scanning flow cell that used the same set of electrodes described in previous segments.[82] The flow cell was connected to a custom-made degasser made of Teflon tubing (AF 2400, Biogeneral, Inc., San Diego, USA) to remove any dissolved gases from the electrolyte. The degasser allowed the gases to permeate from the liquid stream to an electron impact quadrupole mass spectrometer, which was used to analyze the gas composition.

Acknowledgements

This work was funded by the SFB-CRC1316 (grant no. 327886311) and SPP-2370 (grant no. 502202153) of the DFG (German Research Foundation). Further, support by the state of Baden-Württemberg and the DFG through grant no INST 40/574-1 FUGG is gratefully acknowledged. The authors gratefully acknowledge Dr. Thomas Diemant for the XPS measurements. Open Access funding enabled and organized by Projekt DEAL.

Conflict of Interests

The authors declare no conflict of interest.

Data Availability Statement

The data that support the findings of this study are available from the corresponding author upon reasonable request.

Keywords: In-liquid plasma · copper · CO_2 electroreduction · phosphorous-based electrolytes · surface structure

[1] D. Gao, R. M. Arán-Ais, H. S. Jeon, B. Roldan Cuenya, *Nat. Catal.* **2019**, *2*, 19.
[2] Y. Wang, J. Liu, G. Zheng, *Adv. Mater.* **2021**, *33*, 2005798.
[3] R. McGinnis, *Joule* **2020**, *4*, 509.
[4] C. Hepburn, E. Adlen, J. Beddington, E. A. Carter, S. Fuss, N. M. Dowell, J. C. Minx, P. Smith, C. K. Williams, *Nature* **2019**, *575*, 87.
[5] A. Loiudice, P. Lobaccaro, E. A. Kamali, T. Thao, B. H. Huang, J. W. Ager, R. Buonsanti, *Angew. Chem. Int. Ed.* **2016**, *55*, 5789.
[6] A. Vasileff, C. Xu, Y. Jiao, Y. Zheng, S.-Z. Qiao, *Chem* **2018**, *4*, 1809.
[7] P. Ling, Y. Liu, Z. Wang, L. Li, J. Hu, J. Zhu, W. Yan, H. Jiang, Z. Hou, Y. Sun, Y. Xie, *Nano Lett.* **2022**, *22*, 2988.
[8] S. Y. Lee, H. Jung, N.-K. Kim, H.-S. Oh, B. K. Min, Y. J. Hwang, *J. Am. Chem. Soc.* **2018**, *140*, 8681.
[9] K. Jiang, Y. Huang, G. Zeng, F. M. Toma, W. A. Goddard, A. T. Bell, *ACS Energy Lett.* **2020**, *5*, 1206.
[10] P. de Luna, R. Quintero-Bermudez, C.-T. Dinh, M. B. Ross, O. S. Bushuyev, P. Todorović, T. Regier, S. O. Kelley, P. Yang, E. H. Sargent, *Nat. Catal.* **2018**, *1*, 103.
[11] W. Ma, S. Xie, T. Liu, Q. Fan, J. Ye, F. Sun, Z. Jiang, Q. Zhang, J. Cheng, Y. Wang, *Nat. Catal.* **2020**, *3*, 478.
[12] F. Scholten, I. Sinev, M. Bernal, B. Roldan Cuenya, *ACS Catal.* **2019**, *9*, 5496.
[13] R. Reske, H. Mistry, F. Behafarid, B. Roldan Cuenya, P. Strasser, *J. Am. Chem. Soc.* **2014**, *136*, 6978.
[14] G. O. Larrazábal, A. J. Martín, J. Pérez-Ramírez, *J. Phys. Chem. Lett.* **2017**, *8*, 3933.
[15] H. Tabassum, X. Yang, R. Zou, G. Wu, *Chem Catal.* **2022**, *2*, 1561.
[16] C. Reller, R. Krause, E. Volkova, B. Schmid, S. Neubauer, A. Rucki, M. Schuster, G. Schmid, *Adv. Energy Mater.* **2017**, *7*, 1602114.
[17] F. Dattila, R. García-Muelas, N. López, *ACS Energy Lett.* **2020**, *5*, 3176.
[18] D. Cheng, Z.-J. Zhao, G. Zhang, P. Yang, L. Li, H. Gao, S. Liu, X. Chang, S. Chen, T. Wang, G. A. Ozin, Z. Liu, J. Gong, *Nat. Commun.* **2021**, *12*, 395.
[19] A. Verdaguer-Casadevall, C. W. Li, T. P. Johansson, S. B. Scott, J. T. McKeown, M. Kumar, I. E. L. Stephens, M. W. Kanan, I. Chorkendorff, *J. Am. Chem. Soc.* **2015**, *137*, 9808.
[20] H. Mistry, A. S. Varela, C. S. Bonifacio, I. Zegkinoglou, I. Sinev, Y.-W. Choi, K. Kisslinger, E. A. Stach, J. C. Yang, P. Strasser, B. R. Cuenya, *Nat. Commun.* **2016**, *7*, 12123.
[21] A. Eilert, F. Cavalca, F. S. Roberts, J. Osterwalder, C. Liu, M. Favaro, E. J. Crumlin, H. Ogasawara, D. Friebel, L. G. M. Pettersson, A. Nilsson, *J. Phys. Chem. Lett.* **2017**, *8*, 285.
[22] M. Ma, K. Djanashvili, W. A. Smith, *Angew. Chem. Int. Ed.* **2016**, *55*, 6680.
[23] X. Feng, K. Jiang, S. Fan, M. W. Kanan, *ACS Cent. Sci.* **2016**, *2*, 169.
[24] J.-J. Velasco-Velez, R. V. Mom, L.-E. Sandoval-Diaz, L. J. Falling, C.-H. Chuang, D. Gao, T. E. Jones, Q. Zhu, R. Arrigo, B. Roldan Cuenya, A. Knop-Gericke, T. Lunkenbein, R. Schlögl, *ACS Energy Lett.* **2020**, *5*, 2106.
[25] F. Dattila, R. García-Muelas, N. López, *ACS Energy Lett.* **2020**, *5*, 3176.
[26] C. Hahn, T. Hatsukade, Y.-G. Kim, A. Vailionis, J. H. Baricuatro, D. C. Higgins, S. A. Nitopi, M. P. Soriaga, T. F. Jaramillo, *Proc. Nat. Acad. Sci.* **2017**, *114*, 5918.
[27] E. Artmann, P. V. Menezes, L. Forschner, M. M. Elnagar, L. A. Kibler, T. Jacob, A. K. Engstfeld, *ChemPhysChem* **2021**, *22*, 2429.
[28] A. Altaweel, T. Gries, S. Migot, P. Boulet, A. Mézin, T. Belmonte, *Surf. Coat. Technol.* **2016**, *305*, 254.
[29] E. Artmann, L. Forschner, K. M. Schüttler, M. Al-Shakran, T. Jacob, A. K. Engstfeld, *ChemPhysChem* **2022**, *24*, e202200645.
[30] P. V. Menezes, M. M. Elnagar, M. Al-Shakran, M. J. Eckl, P. W. Menezes, L. A. Kibler, T. Jacob, *Adv. Funct. Mater.* **2022**, *32*, 2107058.
[31] H. Yang, P. V. Menezes, G. Dai, G. Vijaykumar, Z. Chen, M. Al-Shakran, T. Jacob, M. Driess, P. W. Menezes, *Appl. Catal. B* **2023**, *324*, 122249.
[32] M. Kaseem, S. Fatimah, N. Nashrah, Y. G. Ko, *Prog. Mater. Sci.* **2021**, *117*, 100735.
[33] J. N. Hausmann, P. V. Menezes, G. Vijaykumar, K. Laun, T. Diemant, I. Zebger, T. Jacob, M. Driess, P. W. Menezes, *Adv. Energy Mater.* **2022**, *12*, 2202098.
[34] D.-W. Kim, B. Lee, D.-W. Park, *J. Electrochem. Soc.* **2019**, *166*, C3200.
[35] T. Li, X. Nie, *ACS Appl. Mater. Interfaces* **2018**, *10*, 16943.
[36] X. Lu, C. Blawert, M. L. Zheludkevich, K. U. Kainer, *Corros. Sci.* **2015**, *101*, 201.
[37] X. Lu, C. Blawert, Y. Huang, H. Ovri, M. L. Zheludkevich, K. U. Kainer, *Electrochim. Acta* **2016**, *187*, 20.
[38] D. Gao, I. Zegkinoglou, N. J. Divins, F. Scholten, I. Sinev, P. Grosse, B. Roldan Cuenya, *ACS Nano* **2017**, *11*, 4825.
[39] C. Quan, Y. He, *Appl. Surf. Sci.* **2015**, *353*, 1320.
[40] C. Zhao, W. Zha, R. Cai, X. Nie, J. Tjong, *ACS Sustainable Chem. Eng.* **2019**, *7*, 5524.
[41] S. K. sen Gupta, R. Singh, *Plasma Sources Sci. Technol.* **2016**, *26*, 015005.
[42] H. Zhu, C. Zhang, Y. Yin, *J. Cryst. Growth.* **2004**, *270*, 722.
[43] S.-C. Lu, M.-C. Hsiao, M. Yorulmaz, L.-Y. Wang, P.-Y. Yang, S. Link, W.-S. Chang, H.-Y. Tuan, *Chem. Mater.* **2015**, *27*, 8185–8188.
[44] Y. Moreno, A. Vega, S. Ushak, R. Baggio, O. Peña, E. le Fur, J.-Y. Pivan, E. Spodine, *J. Mater. Chem.* **2003**, *13*, 2381.
[45] W. Moehl, A. Schweiger, H. Motschi, *Inorg. Chem.* **1990**, *29*, 1536.
[46] S. Ghose, *Acta Crystallogr.* **1963**, *16*, 124.
[47] J. Zhao, L. Sun, S. Canepa, H. Sun, M. N. Yesibolati, M. Sherburne, R. Xu, T. Sritharan, J. S. C. Loo, J. W. Ager III, J. Barber, K. Mølhave, Z. J. Xu, *J. Mater. Chem. A* **2017**, *5*, 11905.
[48] Z. Wei, T. Xia, J. Ma, J. Dai, W. Feng, Q. Wang, P. Yan, *Trans. Nonferrous Met. Soc. China* **2006**, *16*, 168.
[49] Y. Xia, X. Xia, H.-C. Peng, *J. Am. Chem. Soc.* **2015**, *137*, 7947.
[50] Q. Qian, F. Wang, X. Zhang, Q. Zhao, *Inorg. Chem. Commun.* **2021**, *127*, 108555.
[51] P. Jiang, D. Prendergast, F. Borondics, S. Porsgaard, L. Giovanetti, E. Pach, J. Newberg, H. Bluhm, F. Besenbacher, M. Salmeron, *J. Chem. Phys.* **2013**, *138*, 024704.
[52] S. Poulston, P. M. Parlett, P. Stone, M. Bowker, *Surf. Interface Anal.* **1996**, *24*, 811.
[53] E. J. Broadhead, A. Monroe, K. M. Tibbetts, *Langmuir* **2021**, *37*, 3740.
[54] A. Majjane, A. Chahine, M. Et-tabirou, B. Echchahed, T.-O. Do, P. M. Breen, *Mater. Chem. Phys.* **2014**, *143*, 779.
[55] M. M. Elnagar, T. Jacob, L. A. Kibler, *Electrochem. Sci. Adv.* **2021**, *2*, e2100175.
[56] M. M. Elnagar, J. M. Hermann, T. Jacob, L. A. Kibler, *Curr. Opin. Electrochem.* **2021**, *27*, 100696.
[57] M. M. Elnagar, L. A. Kibler, T. Jacob, *Green Chem.* **2023**, *25*, 6238–6252.
[58] A. H. M. da Silva, S. J. Raaijman, C. S. Santana, J. M. Assaf, J. F. Gomes, M. T. M. Koper, *J. Electroanal. Chem.* **2021**, *896*, 115609.
[59] A. Tiwari, H. H. Heenen, A. S. Bjørnlund, T. Maagaard, E. Cho, I. Chorkendorff, H. H. Kristoffersen, K. Chan, S. Horch, *J. Phys. Chem. Lett.* **2020**, *11*, 1450.
[60] S. J. Raaijman, N. Arulmozhi, A. H. M. da Silva, M. T. M. Koper, *J. Electrochem. Soc.* **2021**, *168*, 096510.
[61] M. M. Elnagar, L. A. Kibler, T. Jacob, *J. Electrochem. Soc.* **2022**, *169*, 102509.
[62] A. Bagger, R. M. Arán-Ais, J. Halldin Stenlid, E. Campos dos Santos, L. Arnarson, K. Degn Jensen, M. Escudero-Escribano, B. Roldan Cuenya, J. Rossmeisl, *ChemPhysChem* **2019**, *20*, 3096.
[63] F. L. P. Veenstra, N. Ackerl, A. J. Martín, J. Pérez-Ramírez, *Chem* **2020**, *6*, 1707.
[64] A. Dutta, M. Rahaman, N. C. Luedi, M. Mohos, P. Broekmann, *ACS Catal.* **2016**, *6*, 3804.
[65] H. S. Jeon, S. Kunze, F. Scholten, B. Roldan Cuenya, *ACS Catal.* **2018**, *8*, 531.
[66] K. P. Kuhl, E. R. Cave, D. N. Abram, T. F. Jaramillo, *Energy Environ. Sci.* **2012**, *5*, 7050.
[67] P. Khanipour, M. Löffler, A. M. Reichert, F. T. Haase, K. J. J. Mayrhofer, I. Katsounaros, *Angew. Chem. Int. Ed.* **2019**, *58*, 7273.
[68] O. Piqué, M. Löffler, I. Katsounaros, F. Calle-Vallejo, *Electrochim. Acta* **2021**, *380*, 138247.
[69] Y. Hori, A. Murata, R. Takahashi, *J. Chem. Soc. Faraday Trans. 1* **1989**, *85*, 2309.
[70] H. Chen, Z. Wang, X. Wei, S. Liu, P. Guo, P. Han, H. Wang, J. Zhang, X. Lu, B. Wei, *Appl. Surf. Sci.* **2021**, *544*, 148965.
[71] Y. Huang, Y. Chen, T. Cheng, L.-W. Wang, W. A. Goddard, *ACS Energy Lett.* **2018**, *3*, 2983.
[72] T. Cheng, H. Xiao, W. A. Goddard, *J. Am. Chem. Soc.* **2017**, *139*, 11642.
[73] Y. Hori, H. Wakebe, T. Tsukamoto, O. Koga, *Surf. Sci.* **1995**, *335*, 258.

[74] I. Takahashi, O. Koga, N. Hoshi, Y. Hori, *J. Electroanal. Chem.* **2002**, *533*, 135.
[75] L. Wang, D. C. Higgins, Y. Ji, C. G. Morales-Guio, K. Chan, C. Hahn, T. F. Jaramillo, *Proc. Nat. Acad. Sci.* **2020**, *117*, 12572.
[76] G. L. De Gregorio, T. Burdyny, A. Loiudice, P. Iyengar, W. A. Smith, R. Buonsanti, *ACS Catal.* **2020**, *10*, 4854.
[77] X. K. Lu, B. Lu, H. Li, K. Lim, L. C. Seitz, *ACS Catal.* **2022**, *12*, 6663.
[78] P. Iyengar, J. Huang, G. L. De Gregorio, C. Gadiyar, R. Buonsanti, *Chem. Commun.* **2019**, *55*, 8796.
[79] A. Loiudice, P. Lobaccaro, E. A. Kamali, T. Thao, B. H. Huang, J. W. Ager, R. Buonsanti, *Angew. Chem. Int. Ed.* **2016**, *55*, 5789.
[80] H. Han, Y. Noh, Y. Kim, S. Park, W. Yoon, D. Jang, S. M. Choi, W. B. Kim, *Green Chem.* **2020**, *22*, 71.
[81] S. Nitopi, E. Bertheussen, S. B. Scott, X. Liu, A. K. Engstfeld, S. Horch, B. Seger, I. E. L. Stephens, K. Chan, C. Hahn, J. K. Nørskov, T. F. Jaramillo, I. Chorkendorff, *Chem. Rev.* **2019**, *119*, 7610.
[82] M. Löffler, P. Khanipour, N. Kulyk, K. J. J. Mayrhofer, I. Katsounaros, *ACS Catal.* **2020**, *10*, 6735.

Manuscript received: June 28, 2023
Revised manuscript received: August 1, 2023
Accepted manuscript online: August 6, 2023
Version of record online: ■■, ■■

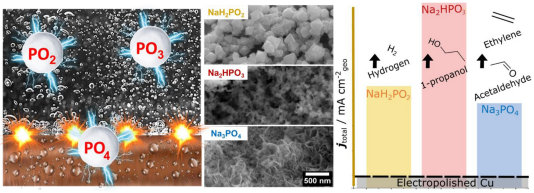

Plasma electrolysis of Cu electrodes in P-based electrolytes generates distinct surface structures, including octahedral nanocrystals, besides nanoporous and microporous features. Cu electrodes polarized in Na_2HPO_3 and Na_3PO_4 exhibit high selectivity for C_2 products, establishing in-liquid plasma as an attractive option for developing efficient Cu electrocatalysts for sustainable CO_2 conversion.

*M. M. Elnagar, Dr. P. V. Menezes, W. A. Parada, Y. Mattausch, Dr. L. A. Kibler, Prof. Dr. K. J. J. Mayrhofer, Prof. Dr. T. Jacob**